Geosci. Model Dev., 14, 6135–6153, 2021
https://doi.org/10.5194/gmd-14-6135-2021

Geoscientific Model Development
Open Access
EGU

Influence on the temperature estimation of the planetary boundary layer scheme with different minimum eddy diffusivity in WRF v3.9.1.1

Hongyi Ding[1], Le Cao[1], Haimei Jiang[1], Wenxing Jia[1,3], Yong Chen[2], and Junling An[2]

[1]Key Laboratory for Aerosol-Cloud-Precipitation of China Meteorological Administration, Nanjing University of Information Science and Technology, Nanjing 210044, China
[2]State Key Laboratory of Atmospheric Boundary Layer Physics and Atmospheric Chemistry, Institute of Atmospheric Physics, Chinese Academy of Sciences, Beijing 100029, China
[3]Key Laboratory of Atmospheric Chemistry of CMA, Chinese Academy of Meteorological Sciences, Beijing 100081, China

Correspondence: Le Cao (le.cao@nuist.edu.cn)

Received: 4 May 2021 – Discussion started: 11 May 2021
Revised: 8 September 2021 – Accepted: 20 September 2021 – Published: 12 October 2021

Abstract. The minimum eddy diffusivity ($K_{z\min}$) in the planetary boundary layer (PBL) scheme can influence the model performance when simulating meteorological parameters such as temperature. However, detailed studies on the sensitivities of the simulated temperatures to the settings of $K_{z\min}$ are still lacking. Thus, in this study we evaluated the performance of the ACM2 (Asymmetrical Convective Model version 2) scheme in the WRF (Weather Research and Forecasting) model with different $K_{z\min}$ settings when simulating the spatiotemporal distribution of the temperature in the region of Beijing, China. Five constant values and a function were implemented in the model to calculate $K_{z\min}$, and the simulation results with different $K_{z\min}$ settings were compared and analyzed. The results show that the increase in $K_{z\min}$ leads to an elevation of the 2 m temperature, especially at nighttime. We figured out that the deviation in the 2 m temperature at night is mainly caused by the different estimations of the turbulent mixing under stable conditions in simulation scenarios with different $K_{z\min}$ settings. Moreover, the spatial distribution of the temperature deviation indicates that under various underlying surface categories, the change in $K_{z\min}$ exerts a distinct influence on the prediction of the 2 m temperature. This influence was found to be stronger during the nighttime than during the daytime, in plain areas than in mountain areas, and in urban areas than in non-urban areas. During the night in the urban areas, the influence on the simulated 2 m temperature brought about by the change in $K_{z\min}$ is the strongest. In addition, the model performance using a functional-type $K_{z\min}$ in the ACM2 scheme for capturing the spatiotemporal distribution of the temperature in this region was also compared with that using a constant $K_{z\min}$.

1 Introduction

The planetary boundary layer (PBL) is a thin layer at the bottom of the atmosphere, which responds to a surface change within an hour or less (Stull, 1988). Generally, the height of the PBL is variable in time and space, ranging from hundreds of meters to a few kilometers. Moreover, within the PBL a noticeable diurnal change in the temperature usually occurs, mainly caused by the warming and cooling of the ambient air by the ground surface during the daytime and the nighttime through turbulent mixing. Turbulence in the PBL is an important form of air motion and plays a critical role in vertically diffusing momentum, heat, moisture, and pollutants (Du et al., 2020). Therefore, it is essential to accurately estimate the effects of turbulence on the vertical mixing within the PBL in weather and air quality models.

In numerical models, the vertical mixing caused by turbulence is usually parameterized using PBL closure schemes. An appropriate PBL scheme can precisely capture the properties of the turbulent mixing and the structure of the PBL. At present, many PBL schemes are implemented in numer-

ical models, such as YSU (Hong et al., 2006), MYJ (Janjić, 1994), MRF (Hong and Pan, 1996), ACM (Pleim and Chang, 1992), QNSE (Sukoriansky and Galperin, 2008; Sukoriansky et al., 2006), BouLac (Bougeault and Lacarrere, 1989), the Shin-Hong scheme (Shin and Hong, 2015), TEMF (Angevine, 2005; Angevine et al., 2010), and MYNN-EDMF (Olson et al., 2019). Generally, the PBL schemes can be classified into two types, local and non-local closure schemes. Local closure schemes, such as MYJ and BouLac, are also called K-theory (Stull, 1988). It usually determines the eddy diffusion coefficient from local prognostic variables such as the turbulent kinetic energy (TKE), local gradients of the wind speed, and the potential temperature. However, in this type of PBL scheme, the mixing caused by large eddies is usually not adequately taken into account. As a result, the local closure schemes frequently fail in simulating the unstable boundary layer (Stull, 1988). In order to overcome the shortcomings of the local closure schemes, many non-local closure schemes such as MRF, YSU, Shin-Hong, TEMF, MYNN-EDMF, and ACM have been proposed. In the MRF non-local closure scheme, a counter-gradient correction term is included (Hong and Pan, 1996), representing a contribution from the large-scale eddies to the total fluxes of heat, momentum, and moisture. By comparing the model results with the observational data, Hong and Pan (1996) suggested that the MRF scheme simulates a more realistic structure of the daytime boundary layer than the local closure scheme. Following this, a modified scheme based on MRF named the YSU scheme was proposed (Hong et al., 2006), which treats the entrainment process occurring at the top of the PBL explicitly. It was found that using the YSU scheme tends to increase the boundary layer mixing in the thermally induced free convection regime but tends to decrease the mixing in the mechanically induced forced convection regime (Hong et al., 2006). In 2015, Shin and Hong (2015) proposed a scale-aware scheme named the Shin-Hong scheme. In this scheme, Shin and Hong (2015) introduced a new algorithm to estimate the vertical transport, and thus the transport of the subgrid-scale heat is weakened. As a result, predictions of large-eddy simulations (LESs) can be better fitted. The TEMF (Total Energy Mass-Flux) scheme, proposed by Angevine et al. (2010), is an update of the EDMF (Eddy Diffusivity Mass-Flux) scheme (Angevine, 2005). In the TEMF scheme, the vertical mixing in free convective boundary layers is treated by combining eddy diffusivity and mass flux. In this way, it can estimate the non-local transport in the convective boundary layer more accurately and better represent the connection between dry thermals and cumulus clouds (Angevine et al., 2010). Recently, a non-local scheme named MYNN-EDMF was developed by Olson et al. (2019) by implementing an EDMF approach into the Mellor–Yamada–Nakanishi–Niino (MYNN) local scheme (Nakanishi and Niino, 2009). The EDMF approach adopted in MYNN-EDMF uses a mass-flux scheme to indicate the non-local turbulent mixing of heat, moisture, and momentum under convective conditions. Moreover, MYNN-EDMF defines TKE on mass points instead of at the interface of the grid cell, which makes the advection of TKE possible in this scheme (Olson et al., 2019). Aside from these non-local closure schemes, the ACM (Asymmetrical Convective Model) scheme proposed by Pleim and Chang (1992) is a non-local PBL scheme that assumes that strongly buoyant plumes rise from the surface layer to all levels in the convective boundary layer. It is also assumed in ACM that the downward motion between each adjacent layer is a gradual subsidence process. It was reported that the ACM scheme can improve the accuracy of the model in capturing the diffusion of chemicals released from elevated sources (Pleim and Chang, 1992). Based on this, by combining the original ACM with a local eddy diffusion module, Pleim (2007a, b) proposed the Asymmetrical Convective Model version 2 (ACM2) scheme to better represent both the super-grid and sub-grid components of the turbulent mixing in the convective boundary layer. They found that adding the local eddy diffusion module into the original ACM exerts a significant impact on quantities that have large surface fluxes, such as the momentum and the heat (Pleim, 2007a, b).

Many researchers have evaluated the performance of available PBL closure schemes under different meteorological conditions (Hu et al., 2010; Xie et al., 2012; Madala et al., 2014; Banks et al., 2016; Gunwani and Mohan, 2017). Generally, they found that during the PBL collapse and at nighttime, the PBL schemes have difficulty precisely capturing the change in meteorological parameters such as the temperature. Moreover, they attributed the biases to the following three aspects. (1) The first being inaccurate calculation of the surface cooling rate. Chaouch et al. (2017) intercompared the performance of seven different PBL schemes in WRF (Weather Research and Forecasting) model (Skamarock et al., 2008) under foggy conditions in the United Arab Emirates. They found a cold bias in the 2 m air temperature during the PBL collapse and at nighttime, reflecting an overestimation of the surface cooling rate. Cuchiara et al. (2014) employed the WRF-Chem (WRF with Chemistry) model (Grell et al., 2005) to analyze the differences in the ozone prediction by four PBL schemes (YSU, ACM2, MYJ, QNSE). In their study, by comparing the model results with the observations, they found that the YSU scheme is in the best agreement with the observed ozone. Moreover, it was found by Cuchiara et al. (2014) that all four of these PBL schemes predict a lower surface cooling rate, thus leading to an underestimation of the temperature by 2–3 K during the PBL collapse and the nighttime. (2) The second aspect involved is unrealistic thermal coupling between the ambient air and the underlying surface in simulations. Udina et al. (2016) studied the vertical structure of a neutral and a stable PBL using the WRF-LES (WRF with Large Eddy Simulation) modeling system (Moeng et al., 2007). They suggested that in the model the calculated thermal coupling at the surface is unrealistically large. As a result, the rate dif-

ference between the molecular thermal conduction and the vertical eddy diffusion is underestimated, leading to the prediction of a lower air temperature near the cooling surface in simulations. It also leads to the formation of a more stable boundary layer compared to the observations. (3) The final aspect is the difference between the internal properties of the PBL schemes. Shin and Hong (2011) numerically investigated the PBL properties using five PBL schemes (YSU, ACM2, MYJ, QNSE, BouLac) in WRF for a day during the Cooperative Atmosphere–Surface Exchange Study (CASES-99) field campaign (Poulos et al., 2002). They found that the simulated surface temperature and the 2 m temperature at nighttime given by these five PBL schemes show positive biases compared with the observations. In addition, they stated that the values of the minimum eddy diffusivity given in these PBL schemes are different, influencing the simulation results.

The minimum eddy diffusivity (K_{z0} or $K_{z\min}$) is a small value to fix the estimation of the vertical eddy diffusivity (K_z) used by the PBL closure schemes. It denotes a weak vertical diffusion in the free atmosphere or a strongly stable boundary layer that cannot be resolved by the model. Li and Rappenglueck (2018) investigated the causes behind the nighttime ozone biases in a simulation of the ground-level ozone in southeastern Texas using the ACM2 scheme in CMAQ (Byun and Schere, 2006). They also compared the results using two different $K_{z\min}$ settings. One setup is that the $K_{z\min}$ is set as a constant value $1\,m^2\,s^{-1}$ across the modeling domain, and the other setup is that $K_{z\min}$ is computed by a formula so that it resides in a value range of 0.01–$1.0\,m^2\,s^{-1}$. They found that using the $K_{z\min}$ calculated by the formula lowers the nighttime vertical mixing, and the average ozone bias is reduced compared with that using the alternative $K_{z\min}$ setting. Their conclusions suggested that the setup of $K_{z\min}$ is capable of changing the simulation results of the model. Nielsen-Gammon et al. (2010) evaluated the role of many parameters in the ACM2 scheme using WRF model. They found that the variation of $K_{z\min}$ exerts a significant impact on the simulated temperature in the lower troposphere, especially at night. Moreover, Nielsen-Gammon et al. (2010) also suggested that different values of $K_{z\min}$ would cause a change in the intensity of the vertical mixing in the upper troposphere. As a result, different vertical profiles of the temperature and the water vapor were obtained in simulations using various $K_{z\min}$ values, leading to a different prediction of cloud patterns and shortwave radiation.

However, at present detailed studies of the sensitivity of the temperature prediction to $K_{z\min}$ are still lacking. Furthermore, the reasons causing the deviations in the simulated temperature brought by the change in $K_{z\min}$ also need to be clarified. In addition, the effects of changing $K_{z\min}$ on the temperature in areas with different categories of the underlying surface are also unclear. Thus, in this study we performed a WRF model simulation on the meteorological field of the region near Beijing, China, and examined the impact exerted by the change in $K_{z\min}$ on the simulated temperature. We also tried to figure out the mechanism for the change in the simulated temperature. By performing this numerical study, the role of $K_{z\min}$ in the prediction of temperature in the Beijing area of China can be clarified, which helps to determine the appropriate setup of $K_{z\min}$ in temperature simulations across this region.

The structure of the paper is as follows. In Sect. 2, we describe the observational data, model settings, and the PBL scheme used in the present study. In Sect. 3, simulation results and the related discussions are given. Finally, major conclusions achieved in the present study are presented in Sect. 4. Future work is also proposed in this section.

2 Observational data and model settings

In the present study, we first evaluated the performance of the PBL scheme (ACM2) with different $K_{z\min}$ values in simulating observed meteorological parameters and then assessed the connection between the differences in the temperature simulations and the value of $K_{z\min}$. Finally, we used a function to calculate $K_{z\min}$ and examined the performance of ACM2 with this function by comparing it with one using a constant $K_{z\min}$ ($0.01\,m^2\,s^{-1}$).

2.1 Observational data

The observational data used in this study are provided by the Institute of Atmospheric Physics, Chinese Academy of Sciences (IAP, CAS), obtained by a meteorological observation tower and an observational system of surface meteorological parameters. Aside from these sources, data provided by four automatic weather stations (AWSs) (nos. 54433, 54406, 54419, 54501) were also adopted to evaluate the model performance (see Fig. 1 for the locations of the IAP station and the AWSs). The information taken from these observational data are as follows.

The meteorological observation tower of IAP was built in 1979 and consistently serves studies on air pollution, atmospheric boundary layer, and atmospheric turbulent diffusion. The tower is located at 39°58′ N, 116°22′ E and has a height of 325 m. A 15-level (8, 15, 32, 47, 63, 80, 102, 120, 140, 160, 180, 200, 240, 280, 320 m) meteorological gradient observation system is instrumented on the tower and provides data including wind speed, wind direction, temperature, and moisture. The time resolution of the data is 10 min.

The observational system of surface meteorological parameters is instrumented next to the tower and provides the surface data including temperature, relative humidity, pressure, radiation, precipitation, and wind speed and direction. The time resolution of these data is 30 min.

The observational data provided by AWSs include wind speed, wind direction, temperature, moisture, and surface pressure, with a time resolution of 1 h. In the present study,

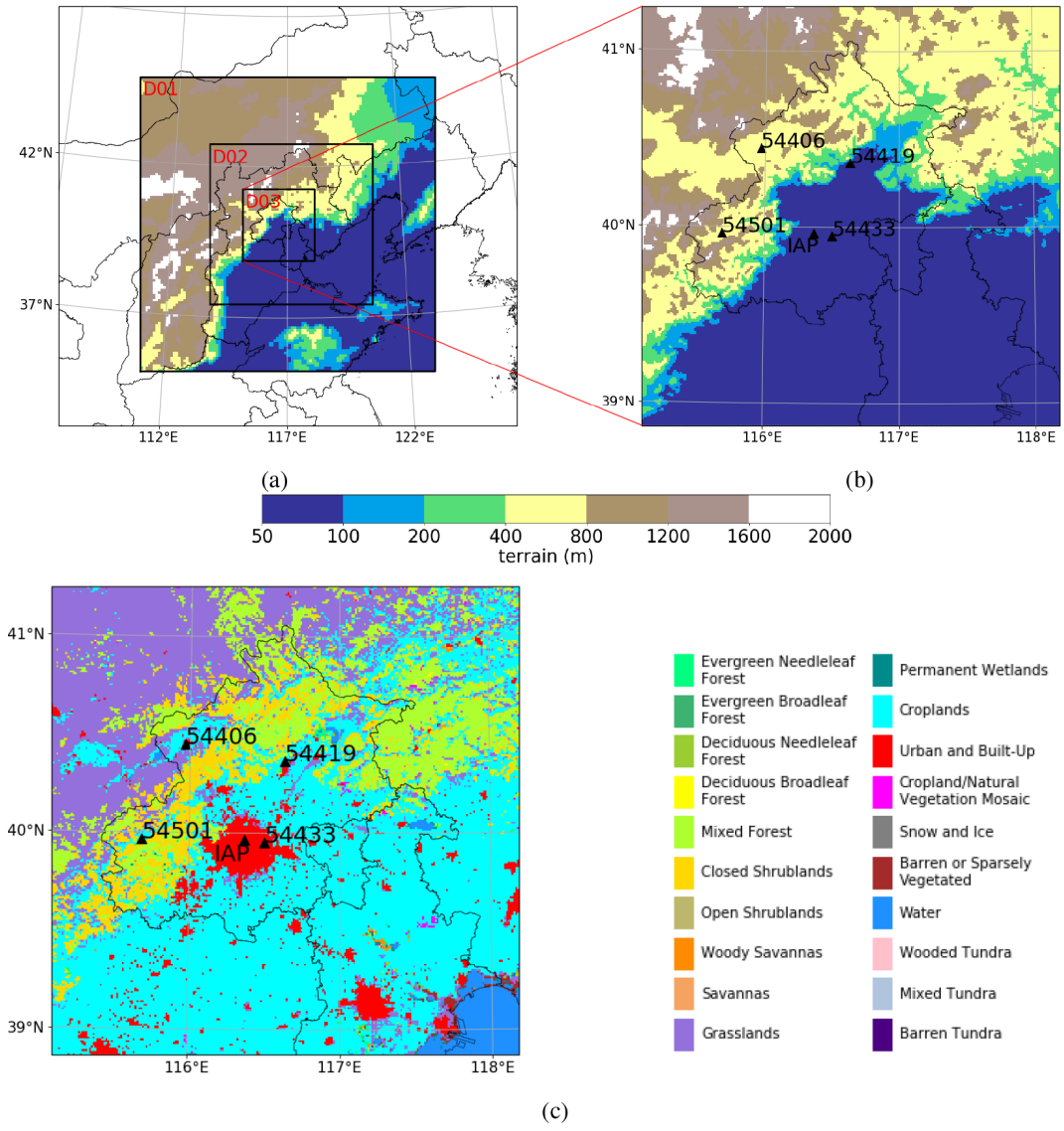

Figure 1. **(a)** Description of the locations of three nested domains, **(b)** an enlarged drawing of the terrain belonging to the innermost domain (i.e., D03), and **(c)** the spatial distribution of the land-use categories within D03. Locations of the IAP station and the four automatic weather stations (nos. 54433, 54406, 54419, 54501) are also marked in **(b)** and **(c)**.

we used the data of 2 m temperature and 10 m wind speed to evaluate the model performance. Among these AWSs, station no. 54433 is located in the urban area of Beijing, similar to the IAP station. In contrast, the other three AWSs (nos. 54406, 54419, 54501) are located in rural or suburban areas of Beijing (see Fig. 1).

2.2 Model description

In this study, we adopted the model WRF-ARW (Advanced Research WRF) version 3.9.1.1 to simulate the meteorological field of the region near Beijing, China. WRF is a mesoscale numerical weather forecasting system designed for atmospheric research and operational forecasting applications. The ARW version is developed and maintained by NCAR (National Center for Atmospheric Research) and is often used for scientific research. In the present study, the WRF model was adapted to the conditions of Beijing and its surrounding areas (Fig. 1). Three nested domains (D01, D02, and D03) were defined (see Fig. 1a), with horizontal grid spacings of 9 km (119×119 grid nodes), 3 km (196×193 grid nodes), and 1 km (259×259 grid nodes), respectively. Along the vertical direction, 48 levels were distributed. The terrain and the categories of the land use in the innermost domain (i.e., D03) are shown in Fig. 1b and c. It is seen that there are mountains in the north (Yan Mountains) and the west (Taihang Mountains) of this area, and the North China Plain is located in the southeast of this studied do-

main. The boundary between the mountain area and the plain area is sharp. In the present study, two time periods (8–15 and 20–24 January 2014) were simulated. In these two time periods, the concentration of $PM_{2.5}$ (particulate matter with diameters smaller than 2.5 µm) accumulates (see Fig. S1 of the Supplement), reflecting relatively stagnant weather conditions in this area. Moreover, these two selected time periods are mostly under sunny conditions, and thus the complexity caused by the existence of clouds is minimized. The impact brought about by the presence of aerosols on the temperature is also not considered in the present study for simplicity. The simulation of each day starts at 08:00 LST (local standard time) of the day before the simulated day, due to the implementation of the spin-up process. The first 16 h were treated as the spin-up time, and results obtained from the following 24 h simulations were analyzed for the present study. Furthermore, the daytime and nighttime in this study are defined as 08:00–17:59 and 18:00–07:59 LST, respectively. The initial and the boundary conditions were given by the $1^\circ \times 1^\circ$ National Centers for Environmental Prediction (NCEP) Global Forecast System (GFS) Final (FNL) gridded analysis datasets (National Centers for Environmental Prediction, National Weather Service, NOAA, U.S. Department of Commerce, 2000) and the Moderate Resolution Imaging Spectroradiometer (MODIS) dataset (Broxton et al., 2014) including 20 land-use categories. The parameterizations used in the present model are listed in Table 1.

2.2.1 ACM2 PBL scheme

In this study, we adopted the ACM2 scheme as the PBL scheme. The reason for choosing ACM2 is that this scheme is included in many numerical models, such as WRF (Skamarock et al., 2008) and CMAQ (Byun and Schere, 2006), and the settings of $K_{z\min}$ in this scheme are given differently in these models, which will be described in a later context. The form of the scalar transport equation in ACM2 is as follows (Pleim, 2007a, b):

$$\frac{\partial C_i}{\partial t} = f_{\text{conv}}\text{Mu}C_1 - f_{\text{conv}}\text{Md}_i C_i + f_{\text{conv}}\text{Md}_{i+1}C_{i+1}\frac{\Delta z_{i+1}}{\Delta z_i} + \frac{\partial}{\partial z}\left[K_c\,(1-f_{\text{conv}})\,\frac{\partial C_i}{\partial z}\right], \quad (1)$$

$$f_{\text{conv}} = \frac{K_h \gamma_h}{K_c \gamma_h - K_h \frac{\partial \theta}{\partial z}}, \quad (2)$$

where C_i is the predicted variable, such as the potential temperature in the ith layer. Mu is the mixing rate of the non-local upward convection, and Md is the rate of the non-local downward mixing from the ith layer to the $(i-1)$th layer. Δz_i is the thickness of the ith model layer. f_{conv} is a ratio factor weighting different contributions from non-local mixing and local mixing, and θ in Eq. (2) is the potential temperature. When the boundary layer is stable or neutral, the ACM2 scheme is mostly dominated by the local transport process, which is represented by the last term on the right-hand side of Eq. (1). By adding the local transport term, the ACM2 scheme improves upon the ACM scheme in capturing the upward turbulent transport process within the boundary layer (Pleim, 2007a, b).

2.2.2 Setup of $K_{z\min}$ in ACM2

In the ACM2 scheme instrumented in the WRF model, $K_{z\min}$ is set as $0.01\ \text{m}^2\ \text{s}^{-1}$ by default. In contrast, in other numerical models such as CMAQ (Byun and Schere, 2006), $K_{z\min}$ is usually given a value between 0.001 and $1.0\ \text{m}^2\ \text{s}^{-1}$. Thus, in order to clarify the differences in simulation results caused by the variation of $K_{z\min}$, five simulation scenarios with different constant values of $K_{z\min}$ were conducted in the present study (see Table 2). In addition, we also performed a simulation using a function to determine $K_{z\min}$ (i.e., ACM2_CMAQ in Table 2). This function was taken from the CMAQ model, shown as follows:

$$Z \le \text{KZMAXL} : K_{z\min} = 0.01 + (1 - 0.01)\text{PURB}, \quad (3)$$

$$Z \ge \text{KZMAXL} : K_{z\min} = 0.01, \quad (4)$$

where

$$\text{KZMAXL} = 500.0\ (\text{m}), \quad (5)$$

$$\text{LU\_INDEX} = \text{LU\_INDEX(Water)} : \text{PURB} = 0, \quad (6)$$

$$\text{LU\_INDEX} \neq \text{LU\_INDEX(Water)} : \text{PURB} = \frac{\text{Landusef(Urban)}}{1 - \text{Landusef(Water)}}. \quad (7)$$

In Eqs. (3)–(7), Z is the height of the layer, and KZMAXL is a prescribed height above which the atmosphere would not be significantly affected by the change in the surface properties. PURB is a percentage ratio of the urbanization. LU_INDEX is an index representing the dominant category of the land use. Landusef is a fraction of each land-use category in the grid cell. The spatial distributions of Landusef and PURB used in the present study are shown in Fig. S2 of the Supplement. By using the function described in Eqs. (3)–(7), the range of $K_{z\min}$ given in the model is between 0.01 and $1\ \text{m}^2\ \text{s}^{-1}$. Moreover, for completely non-urban areas (i.e., PURB = 0.0), the value of $K_{z\min}$ is $0.01\ \text{m}^2\ \text{s}^{-1}$, which is the same as the default value used in the ACM2 scheme of the WRF model, while for completely urban areas (i.e., PURB = 1.0) the value of $K_{z\min}$ below the height of 500 m calculated by Eqs. (3)–(7) is 1.0, the same as that used in the ACM2_1.0 scenario. We then compared the performance of ACM2 adopting this function with that using a constant $K_{z\min}$ ($0.01\ \text{m}^2\ \text{s}^{-1}$) in simulating the temperature in the region of Beijing.

Furthermore, we designed two sensitivity tests in the present study (see Table 2). One of them is AC_night_0.01,

Table 1. Parameterizations used in the present model.

Namelist option	Description	Reference
mp_physics	Purdue Lin scheme	Chen and Sun (2002)
ra_lw_physics	RRTM scheme	Mlawer et al. (1997)
ra_sw_physics	Dudhia scheme	Dudhia (1989)
sf_sfclay_physics	MM5 scheme	Zhang and Anthes (1982)
sf_surface_physics	Noah land surface model	Chen and Dudhia (2001)
bl_pbl_physics	ACM2 scheme	Pleim (2007a, b)
cu_physics	Grell 3D scheme (Domain 1 and 2)	Grell and Dévényi (2002)
sf_urban_physics	Single-layer UCM	Kusaka et al. (2001)

Table 2. Scenarios simulated in the present study with a different setup of $K_{z\min}$ in the ACM2 scheme.

Type	$K_{z\min}$ ($m^2\ s^{-1}$)	Name
Constant	0.01	ACM2_0.01
	0.2	ACM2_0.2
	0.5	ACM2_0.5
	0.8	ACM2_0.8
	1.0	ACM2_1.0
Function	0.01–1.0	ACM2_CMAQ
Sensitivity test	1.0 (daytime), 0.01 (nighttime)	AC_night_0.01
	1.0 (urban), 0.01 (non-urban)	AC_urban_1

in which $K_{z\min}$ was set to 0.01 during the nighttime (same as ACM2_0.01), but 1.0 during the daytime (same as ACM2_1.0). The results of this sensitivity test help to differentiate the contributions by the difference in the simulated nighttime temperature and the change in $K_{z\min}$ during the daytime. The other sensitivity test is AC_urban_1, in which $K_{z\min}$ was set to 1.0 only over urban areas (same as ACM2_1.0), but 0.01 over other areas (same as ACM2_0.01). Through this sensitivity test, the influence brought about by the temperature advection on the near-surface temperature estimation can be indicated, which will be discussed further in a later context.

2.3 Evaluation criterion

In order to evaluate the performance of the model with different settings of $K_{z\min}$, four statistical metrics, index of agreement (IOA) (Willmott, 1982), root-mean-square error (RMSE), correlation coefficient (R), and mean bias (MB) were implemented. These parameters are calculated as follows:

$$\mathrm{IOA} = 1 - \left[\frac{\sum_{i=1}^{N}(P_i - O_i)^2}{\sum_{i=1}^{N}\left(\left|P_i - \overline{O}\right| + \left|O_i - \overline{O}\right|\right)^2}\right], \tag{8}$$

$$\mathrm{RMSE} = \sqrt{\frac{\sum_{i=1}^{N}(P_i - O_i)^2}{N}}, \tag{9}$$

$$R = \frac{\sum_{i=1}^{N}\left(P_i - \overline{P}\right)\left(O_i - \overline{O}\right)}{\sqrt{\sum_{i=1}^{N}\left(P_i - \overline{P}\right)^2}\sqrt{\sum_{i=1}^{N}\left(O_i - \overline{O}\right)^2}}, \tag{10}$$

$$\mathrm{MB} = \frac{\sum_{i=1}^{N}(P_i - O_i)}{N}, \tag{11}$$

where N is the amount of data, O is the observed value, and P is the value predicted by the model. $\overline{O}$ and $\overline{P}$ denote the average values of these variables. RMSE, R, and MB are common statistical parameters, and IOA is a metric evaluating the fitness between model predictions and observations. When IOA is equal to 1, it represents a perfect match, while IOA = 0 denotes that no agreement is achieved.

3 Results and discussion

In Sect. 3.1, the performance of the model in simulating the 2 m temperature and 10 m wind speed is evaluated and displayed. In Sect. 3.2, we show the impact of changing $K_{z\min}$ on the 2 m temperature and discover the reasons for the change in the 2 m temperature. In Sect. 3.3, the effect of changing $K_{z\min}$ under different underlying surface categories is shown. In Sect. 3.4, we compare the performance of ACM2 adopting the function described in Eqs. (3)–(7) with the results using the constant $K_{z\min}$ 0.01 $m^2\ s^{-1}$.

3.1 Model evaluation

The simulation results of the 2 m temperature and the 10 m wind speed were compared with the observational data provided by the above-mentioned IAP, CAS station, and four automatic weather stations (AWSs) to evaluate the model performance. The values of statistical parameters measuring the model performance are listed in Table 3. Generally speaking, the model behavior in capturing the 2 m temperature is sat-

isfying. The correlation coefficients between the simulated temperature and the observations at these five stations reside in a value range of 0.78–0.94. Moreover, the index of agreement (i.e., IOA) also possesses a value above 0.75 for all five stations. It was also found that the model performs better at the two urban stations (IAP and no. 54433) than at the other three rural stations, denoted by a smaller RMSE and a higher R (see Table 3). More information about the comparison between the simulated 2 m temperature and the observations at these five stations can be found in Sect. S3 of the Supplement.

Compared with the temperature estimation, the model predicts a higher wind speed at all five stations (see MB of W10 in Table 3). The deviation between the simulation result and the observational data is more pronounced at the IAP station, as it possesses the largest MB of 2.51 m/s. Moreover, according to the correlation coefficient R, the simulated trend of the 10 m wind speed at two urban stations (IAP and no. 54433) is more consistent with the observations than that at the rural stations, as the correlation coefficient R at these two urban stations is above 0.6. More information about the simulated 10 m wind speed across the computational domain can also be found in Sect. S3 of the Supplement.

Many factors can cause the deviation between the simulation results and the observational data, such as the uncertainties brought about by the imposed inaccurate initial and boundary conditions and the treatment of aerosols in the model and the choice of PBL schemes. However, the main objective of the present study is to estimate the influence caused by the change in $K_{z\min}$ on the prediction of the temperature, rather than finding an improved PBL scheme that can more accurately reproduce the observations. Moreover, the change in $K_{z\min}$ exerts a more significant influence on the temperature than other meteorological parameters such as the wind speed and the specific humidity (see Sect. S4 of the Supplement). Thus, we paid more attention to the influence on the temperature prediction brought about by the change in $K_{z\min}$ in the present study.

3.2 Impact of changing $K_{z\min}$ on 2 m temperature

Figure 2 shows the diurnal mean time series of the temperature at 2 m (T2), the surface skin temperature (TSK), and the temperature at the first model layer (T_level1) at the observation site of IAP predicted by ACM2 with different $K_{z\min}$ constant values. In Fig. 2a, it is seen that the highest T2 appears at approximately 15:00 LST (local standard time). At this time, the average T2 estimated by ACM2_0.01 and ACM2_1.0 are 1.81 and 2.25 °C, and T2 estimated by the other scenarios is between these two values. In contrast, the lowest T2 appears at about 08:00 LST. At this time, the average T2 predicted by ACM2_0.01 and ACM2_1.0 are −6.69 and −4.13 °C. Among these scenarios, ACM2_0.01 consistently predicts the lowest T2. Moreover, it was found that the simulated T2 elevates with the increase of $K_{z\min}$. In addition,

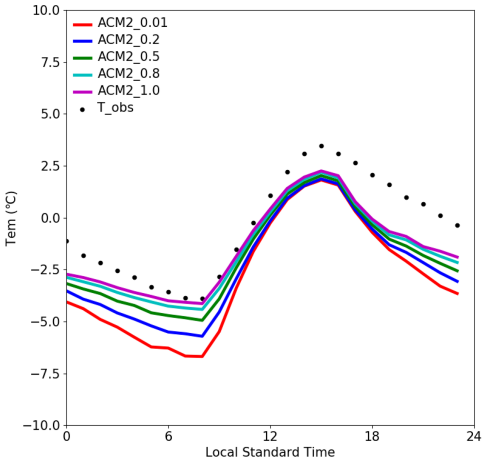

(a) temperature at 2 m (T2)

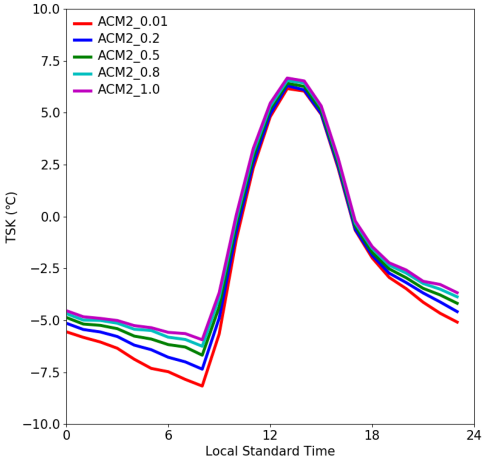

(b) surface skin temperature (TSK)

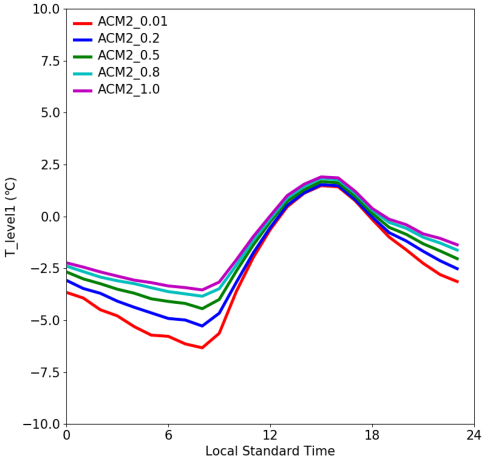

(c) temperature at the first model layer (T_level1)

Figure 2. Diurnal mean time series of **(a)** the temperature at 2 m (T2), **(b)** the surface skin temperature (TSK), and **(c)** the temperature at the first model layer (T_level1) predicted by the ACM2 scheme with different $K_{z\min}$ constant values.

Table 3. Values of statistical parameters measuring the model performance when simulating the 2 m temperature (T2) and the 10 m wind speed (W10) at five observation stations.

	T2				W10			
Station	RMSE	IOA	R	MB	RMSE	IOA	R	MB
IAP	2.79	0.84	0.94	−2.49	3.21	0.26	0.64	2.51
54406	2.84	0.88	0.83	1.06	3.08	0.44	0.50	2.21
54419	3.16	0.85	0.86	1.11	2.28	0.30	0.35	1.49
54433	2.17	0.92	0.91	−1.38	2.40	0.62	0.65	1.26
54501	4.85	0.76	0.78	2.75	2.06	0.52	0.36	0.94

the difference in T2 between these five scenarios is smaller at a higher T2, while the difference becomes larger at a lower T2. As a result, the diurnal variation of T2 is reduced with the increase of $K_{z\min}$.

We then investigated the reasons causing the difference in the simulated T2 between these scenarios. In the model, T2 is calculated based on TSK, the surface sensible heat flux, and the exchange coefficient of temperature at 2 m. Moreover, the sensible heat flux is calculated according to the estimated TSK and the temperature at the first model layer (i.e., T_level1) (Li and Bou-Zeid, 2014). Thus, the estimation of T2 heavily depends on the values of the simulated TSK and T_level1. We thus show the diurnal mean time series of TSK and T_level1 estimated using different $K_{z\min}$ values (see Fig. 2b and c). It can be seen that during nighttime both TSK and T_level1 increase remarkably with the increase of $K_{z\min}$, which is similar to the temporal behavior of T2. This finding also partly agrees with the conclusions of Steeneveld et al. (2006), who stated that TSK increases substantially with an enhanced vertical mixing during the nighttime. However, from the temporal change in these two temperatures, we cannot figure out whether the difference in T2 is mostly caused by the change in the surface temperature (i.e., TSK) or the temperature in the atmosphere (i.e., T_level1) because of the interaction between the surface and the atmosphere. Therefore, we continue to search for the dominant factor causing the change in TSK and T_level1.

We first try to infer the reason causing the difference in TSK from the energy balance equation. In the Noah land surface model (Chen and Dudhia, 2001; Xie et al., 2012) used in this study, when neglecting the precipitation and the snow accumulated on the surface, the form of the energy balance equation is

$$(1-\alpha)\,S\downarrow + L\downarrow - L\uparrow + G - \mathrm{HFX} - LH = 0, \tag{12}$$

where α is the albedo of the underlying surface, $S\downarrow$ is the downward flux of the shortwave radiation, $L\downarrow$ is the downward flux of the longwave radiation emitted by the cloud and the atmosphere, and $L\uparrow$ is the upward flux of the longwave radiation emitted by the ground surface. G is the ground heat flux, and it is positive when heat transfers from the soil to the surface. HFX is the sensible heat flux, and LH is the latent heat flux at the surface. HFX and LH are positive when the heat transfers from the surface to the atmosphere. We then combined $L\downarrow$ and $L\uparrow$ as a net longwave radiation flux ($\mathrm{NL} = L\downarrow - L\uparrow$). As a result, Eq. (12) becomes

$$(1-\alpha)\,S\downarrow + G + \mathrm{NL} - \mathrm{HFX} - LH = 0. \tag{13}$$

Thus, five factors ($S\downarrow$, G, NL, HFX, and LH) need to be evaluated for the difference in TSK between these simulation scenarios. Among these factors, we can first eliminate the shortwave radiation $S\downarrow$ as the dominant factor for the deviation in TSK. This is because in this study the difference in the downward shortwave radiation during the daytime between scenarios using different $K_{z\min}$ values is negligible (see Fig. S6 of the Supplement). This means that the influences exerted by the shortwave radiation in the daytime under the conditions of various $K_{z\min}$ settings are similar. Thus, it cannot result in the enlarged deviation in TSK during the nighttime through the carryover effects. Aside from that, the shortwave radiation at night is negligible. Therefore, we suggested that the shortwave radiation is unimportant for the deviation in the nighttime TSK prediction in the present study. Thus, four factors (G, NL, LH, and HFX) need to be evaluated. Figure 3 shows the temporal profiles of the deviations (ACM2_0.2 minus ACM2_0.01, ACM2_0.5 minus ACM2_0.01, ACM2_0.8 minus ACM2_0.01, ACM2_1.0 minus ACM2_0.01) in G, NL, LH, and HFX given by the model simulations. From Fig. 3a, we can see that during the nighttime the negative deviation in the ground heat flux G becomes larger when $K_{z\min}$ increases, indicating that G is reduced with the increase of $K_{z\min}$ in the nighttime. Because lower G at nighttime indicates that less heat is transferred from the soil to the surface, which cannot lead to a higher TSK; the heat flux from the soil to the surface, G, can also be eliminated as the dominant factor causing the change in TSK during the nighttime. Following this, from Fig. 3b it can be seen that during the nighttime the negative deviation in the net longwave radiation (i.e., NL) becomes larger when $K_{z\min}$ increases, which means that the value of NL also gets reduced when $K_{z\min}$ increases. Lower NL means that the surface loses more longwave radiation energy, which cannot lead to a higher TSK. Thus, it can be deduced that the change in the net longwave radiation flux NL is also not the factor

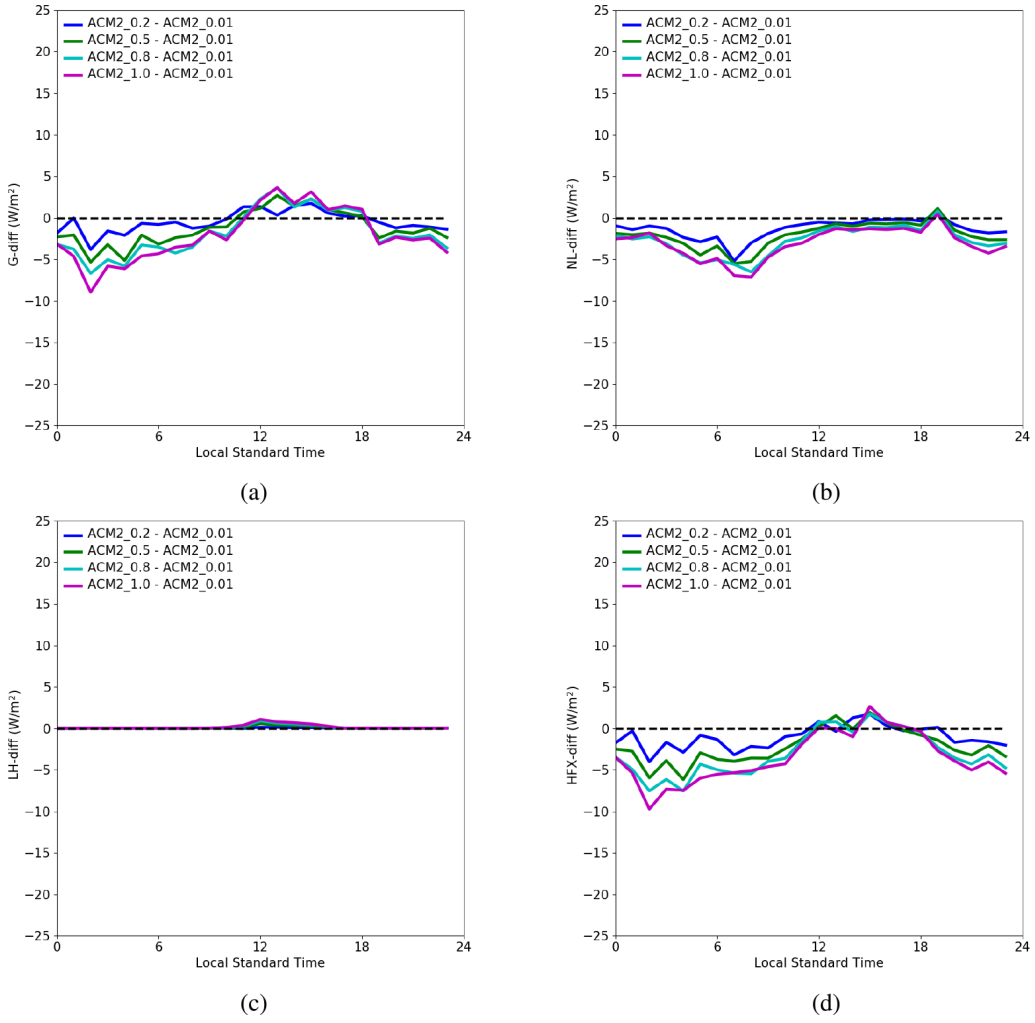

Figure 3. Diurnal mean time series of deviations (based on ACM2_0.01) in **(a)** the ground heat flux G, **(b)** the net longwave radiation flux NL, **(c)** the latent heat flux LH, and **(d)** the sensible heat flux HFX at the surface.

causing the growth of the TSK difference. Figure 3c shows that during the nighttime there is no obvious difference in the latent heat flux LH between these scenarios. Therefore, LH can also be screened out. Finally, Fig. 3d demonstrates that during the nighttime the negative bias in the sensible heat flux HFX becomes larger when $K_{z\min}$ increases, which means that HFX is reduced when $K_{z\min}$ increases. Lower HFX at night means that more heat is transferred from the atmosphere to the underlying surface, which can increase TSK. Thus, we can conclude that the difference in the sensible heat transported from the atmosphere to the ground among these simulation scenarios causes the different growth of TSK during the nighttime in the present simulations.

We then tried to reveal the reasons for the change in the air temperature at the first model layer (i.e., T_level1) caused by the modifications of $K_{z\min}$ in the model. Figure 4 shows averaged vertical profiles of the potential temperature predicted by ACM2 using different $K_{z\min}$ at 08:00 and 15:00 LST. From Fig. 4a, we found that at 08:00 LST, the potential temperature difference at the first model layer is the largest between these five scenarios. When $K_{z\min}$ increases, the predicted near-surface potential temperature elevates. This is consistent with the conclusion of Nielsen-Gammon et al. (2010) that $K_{z\min}$ exerts the most prominent effect during the nighttime, and the variation of $K_{z\min}$ is positively correlated with the change in the near-surface potential temperature. Moreover, seen from Fig. 4a, the potential temperature difference becomes smaller at a higher altitude. Above the height of 400 m, the potential temperature profiles predicted by these five scenarios are almost identical. Therefore, when $K_{z\min}$ increases, the vertical gradient of the mean potential temperature decreases at this time. It is because the PBL becomes stable during the nighttime when the turbulence is very weak. The settings of $K_{z\min}$ thus exert a more significant influence on K_z. As a result, the increase of $K_{z\min}$ would lead to a substantial enhancement of the vertical mix-

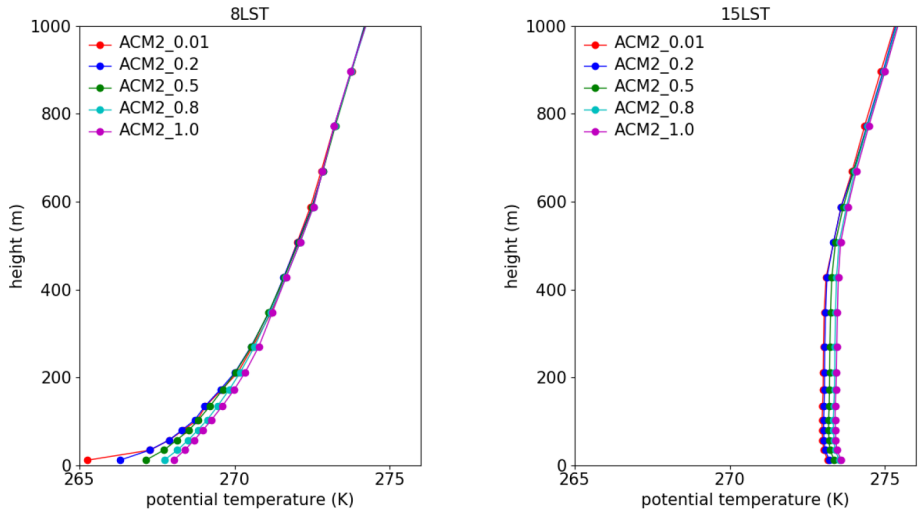

Figure 4. The vertical profiles of the potential temperature predicted by the ACM2 scheme with different $K_{z\mathrm{min}}$ values at **(a)** 08:00 LST and **(b)** 15:00 LST averaged over the simulated days.

ing during the nighttime. This enhanced vertical mixing then causes a more uniform vertical distribution of the potential temperature within the PBL and thus a prediction of a smaller temperature gradient below the top of the PBL. This conclusion also follows Nielsen-Gammon et al. (2010), who stated that the minimum vertical diffusivity is negatively correlated with the temperature gradient during the nighttime.

It should be noted that the difference in the longwave radiation emitted from the ground surface with various TSK is also a possible reason for the deviation in T_level1 between different scenarios. However, a comparison of temperature tendencies caused by the net longwave radiation at the first model layer between scenarios using different $K_{z\mathrm{min}}$ values suggests that the net longwave radiation tends to reduce the nighttime temperature difference between these scenarios instead of enlarging it (see Sect. S6 of the Supplement). Thus, the longwave radiation cannot be the factor causing the enlarged difference in the near-surface temperature between the nighttime simulations.

For the predicted vertical profile of the potential temperature at 15:00 LST, it was found in Fig. 4b that larger $K_{z\mathrm{min}}$ also estimates a higher potential temperature. This deviation between the daytime temperature profiles can be partly attributed to the carryover effects of the significant temperature differences during the nighttime. Aside from that, in the ACM2 scheme $K_{z\mathrm{min}}$ is added to K_z to constitute a total vertical turbulent diffusivity (Pleim, 2007a, b). As a result, even in the daytime when the turbulent diffusion is relatively strong, the change in $K_{z\mathrm{min}}$ can still affect the turbulent mixing, resulting in a deviation in the predicted temperature in the daytime. The contributions of these two processes are to be investigated in a later context. In addition, Fig. 4b shows that the temperature profiles at 15:00 LST are closer to each other than those at 08:00 LST. The reason is that the turbulent intensity is vigorous during the daytime, and thus the change of $K_{z\mathrm{min}}$ has a relatively minor impact on the eddy diffusivity K_z and the vertical distribution of the temperature.

Based on the information given above, we can conclude that the differences in the simulated air temperature during the daytime brought about by the change in $K_{z\mathrm{min}}$ are caused by the combined effect of the large temperature difference during the nighttime and the different turbulent mixing intensity during the daytime. To clarify this, we designed a sensitivity test named AC_night_0.01, in which $K_{z\mathrm{min}}$ was set to 0.01 during the nighttime (same as ACM2_0.01) but 1.0 during the daytime (same as ACM2_1.0). By doing this, contributions to the temperature difference by these two processes can be assessed separately.

The time-averaged vertical profiles of the potential temperature at 08:00 and 15:00 LST are shown in Fig. 5. In Fig. 5a, potential temperature profiles belonging to AC_night_0.01 and ACM2_0.01 were found close to each other due to the same nighttime $K_{z\mathrm{min}}$ values being used in both scenarios. In contrast, in the daytime (see Fig. 5b), AC_night_0.01 was found predicting a higher temperature than ACM2_0.01, which is caused by the increase of $K_{z\mathrm{min}}$ during the daytime and the enhanced turbulent mixing. Meanwhile, AC_night_0.01 was also found to give a lower temperature than ACM2_1.0 during the daytime, although a same $K_{z\mathrm{min}}$ ($= 1.0$) is used during this time period in these two scenarios. Thus, the difference between AC_night_0.01 and ACM2_1.0 denotes the residual effect caused by the temperature difference during the nighttime.

Thus, according to this sensitivity test, we confirmed that there are two primary processes causing the temperature difference during the daytime between scenarios using different

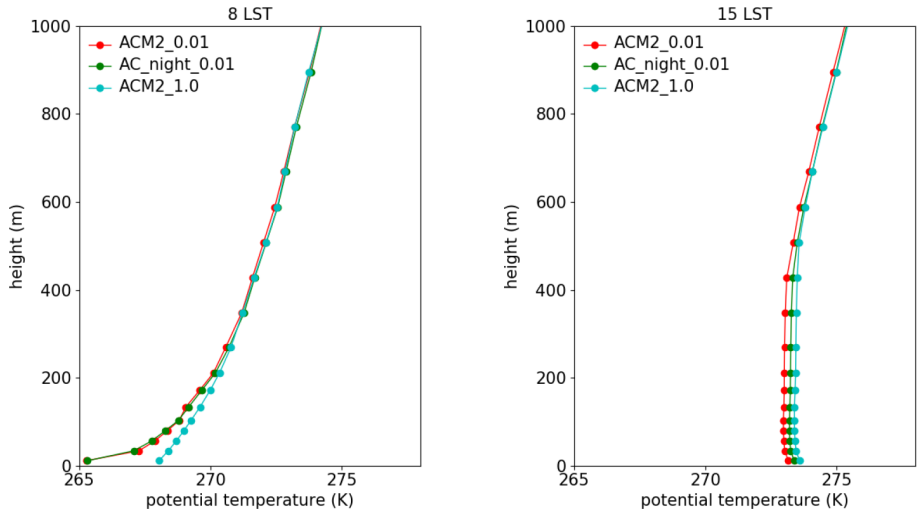

(a) (b)

Figure 5. The vertical profiles of the potential temperature predicted by ACM2_0.01, ACM2_1.0, and AC_night_0.01 at **(a)** 08:00 LST and **(b)** 15:00 LST averaged over the simulated days.

$K_{z\min}$ values. One is the residual effect caused by the change in $K_{z\min}$ in the nighttime. It is because different $K_{z\min}$ results in a large deviation in the near-surface temperature during the nighttime. This deviation would remain until the daytime comes, and thus the prediction of the daytime temperature would be affected. The other process is the change in $K_{z\min}$ in the daytime. When $K_{z\min}$ increases, the vertical mixing in the boundary layer is strengthened, which causes a stronger entrainment of the air from the upper layer into the boundary layer, thus resulting in a warmer boundary layer during the daytime.

This enhanced entrainment caused by the strengthening of the turbulent mixing during the daytime when ACM2 is used is also consistent with findings from previous studies. Unlike many other PBL schemes, ACM2 does not consider the entrainment flux explicitly. Instead, it includes the entrainment implicitly by combining a transilient term with the local mixing that is represented by the maximum of two forms of the turbulent diffusivity (Pleim, 2007a, b). Consequently, when ACM2 is used, the entrainment is very sensitive to the turbulent mixing within and above the PBL. It was also suggested by Nielsen-Gammon et al. (2010) and Hu et al. (2010) that when ACM2 is used, a stronger turbulent mixing in the boundary layer would result in a warmer PBL as well as a cooler free troposphere in the daytime. These conclusions confirm our suggestion in this study that a larger turbulent diffusivity given by ACM2 implementing a higher $K_{z\min}$ leads to a strengthening of the entrainment and thus a warming of the boundary layer during the daytime.

Thus, based on the investigations of TSK and T_level1 discussed above, we can conclude the mechanism causing the remarkable change in T2 between the simulation scenarios with different $K_{z\min}$ settings during the nighttime shown in Fig. 2a. When $K_{z\min}$ increases, the vertical mixing in the nighttime is significantly enhanced. As a result, the near-surface temperature in the boundary layer (i.e., T_level1) is elevated due to the enhanced mixing of the warm air from the atmosphere above. The higher near-surface temperature thus leads to a reduction of the sensible heat flux at the surface (i.e., HFX) in the nighttime and results in an increase of the surface skin temperature (TSK). Because the 2 m air temperature (i.e., T2) calculated in the model is positively dependent on the values of TSK and T_level1, the elevation of $K_{z\min}$ thus causes the increase in T2.

3.3 Impact of changing $K_{z\min}$ under different underlying surface categories

The spatial distributions of the time-averaged differences (ACM2_1.0 minus ACM2_0.01) in T2, TSK, and HFX, as well as the actual values obtained by ACM2_0.01 (the default $K_{z\min}$ in WRF), over the daytime and the nighttime are shown in Fig. 6. From Fig. 6a and b, we can see three distinct features about the influence of increasing $K_{z\min}$ on T2. First, the difference in T2 is mostly larger in plain areas than in mountain areas, which means that the increase of $K_{z\min}$ has a stronger influence on T2 in plain areas than in mountain areas. The reason for the relatively strong impact of changing $K_{z\min}$ in plain areas compared to mountain areas might be attributed to the spatial difference in the simulated near-surface wind speed throughout the computational domain. In Figs. S4 and S8 of the Supplement, we display the spatial distributions of the 10 m wind speed and the friction velocity during the nighttime, which is capable of representing the intensity of the wind shear. It was found that in mountain areas, the 10 m wind speed and the friction velocity are larger

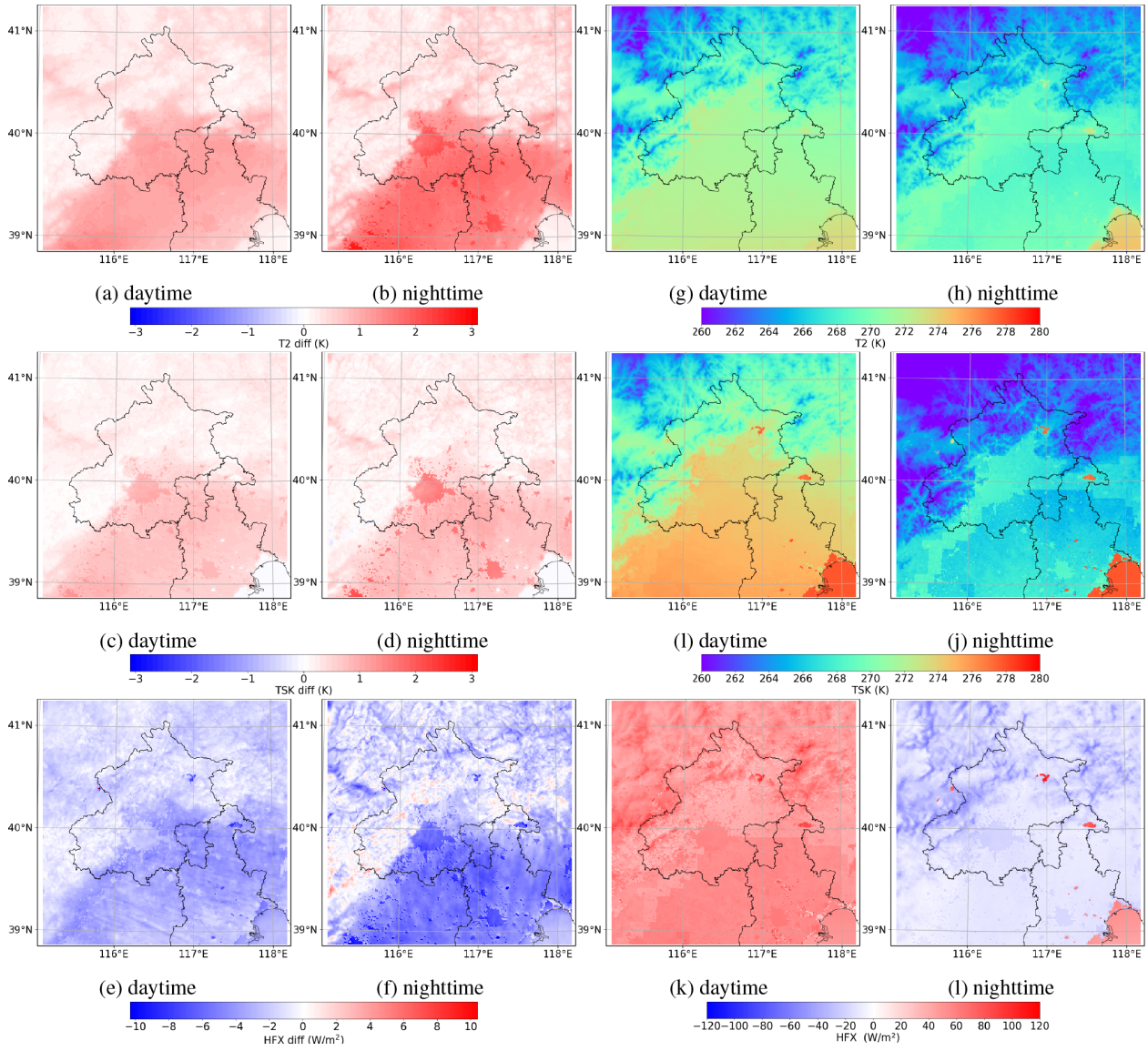

Figure 6. Spatial distribution of the mean difference (ACM2_1.0 minus ACM2_0.01) in **(a, b)** the 2 m temperature (T2), **(c, d)** the surface skin temperature (TSK), and **(e, f)** the sensible heat flux (HFX) over the daytime and the nighttime. The actual values of **(g, h)** T2, **(i, j)** TSK, and **(k, l)** HFX simulated by ACM2 with the default $K_{z\,\mathrm{min}}$ value (i.e., ACM2_0.01) during the daytime and the nighttime are also displayed for reference.

compared to those in plain areas. This means that in mountain areas a stronger wind shear is formed, which causes an enhancement of the turbulent mixing in the nocturnal boundary layer. Thus, a larger turbulent diffusivity was found in mountain areas than in plain areas (shown in Fig. S9 of the Supplement). As a result, elevating $K_{z\,\mathrm{min}}$ in the mountain areas exerts a relatively minor influence on the vertical mixing in the boundary layer and the simulated T2. Second, it was found that in plain areas the difference in T2 is mostly larger during the nighttime than during the daytime, denoting a stronger impact on T2 exerted by the increase of $K_{z\,\mathrm{min}}$ during the nighttime than during the daytime. Third, from the comparison between Fig. 6a and b, it was found that during the nighttime the difference in T2 is substantially larger in urban and built-up areas than in areas in other land-use categories. However, during the daytime the difference is smaller. This means that the increase of $K_{z\,\mathrm{min}}$ has the strongest influence on T2 in urban and built-up areas during the nighttime. The reason why $K_{z\,\mathrm{min}}$ plays a more important role in urban areas than in rural areas in the present study still needs further investigation. We guessed that it might be caused by the difference in physical properties (e.g., heat capacity) between areas with different land-use categories or the difference in

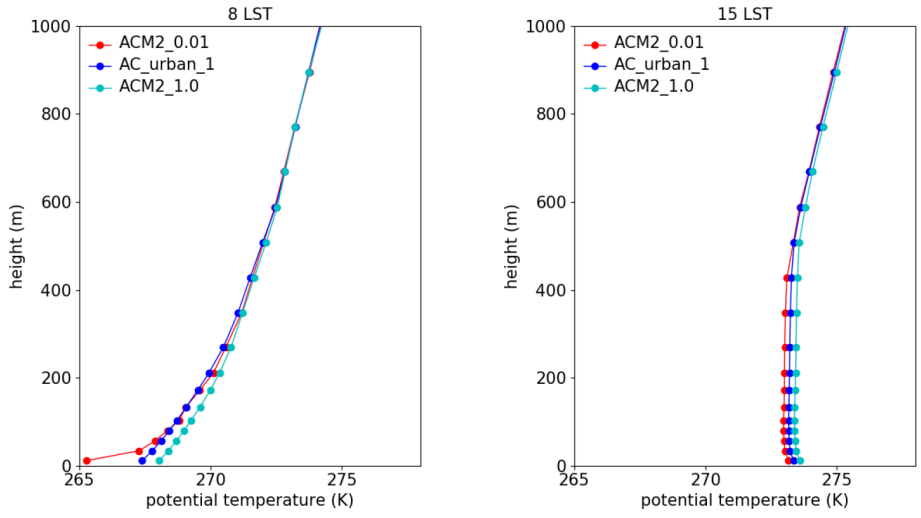

(a) (b)

Figure 7. The vertical profiles of the potential temperature predicted by ACM2_0.01, AC_urban_1, and ACM2_1.0 at **(a)** 08:00 LST and **(b)** 15:00 LST averaged over the simulated days.

parameterizations of some physical processes in the urban canopy model.

The different role of $K_{z\min}$ in urban and rural areas is also able to modify the horizontal advection of temperature across the computational domain, thus affecting the near-surface temperature prediction at the observation site. In order to clarify this, we designed another numerical experiment named AC_urban_1, in which $K_{z\min}$ was set to 1.0 only over urban areas (the same as ACM2_1.0) but 0.01 over other areas (the same as ACM2_0.01). By doing this, the influence brought about by the temperature advection on the near-surface temperature estimation can be indicated.

The time-averaged vertical profiles of the potential temperature at the observation site (i.e., IAP station) at 08:00 and 15:00 LST are shown in Fig. 7. It was found that although AC_urban_1 and ACM2_1.0 possess the same value of $K_{z\min}$ for the urban areas that are focused on in this study, AC_urban_1 still estimates a lower nighttime temperature than ACM2_1.0 (see Fig. 7a) due to the smaller $K_{z\min}$ over rural areas. We suggested the reason as that lower $K_{z\min}$ over rural areas in AC_urban_1 causes a weaker turbulent mixing and thus a lower near-surface temperature in rural areas than those given by ACM2_1.0. This difference in the near-surface temperature of rural areas consequently affects the temperature prediction over urban areas through the advection process. In contrast, the nighttime temperature difference between AC_urban_1 and ACM2_0.01 shown in Fig. 7a can be mostly attributed to the stronger turbulent mixing over urban areas in AC_urban_1 relative to that in ACM2_0.01. Because of this, the vertical gradient of the near-surface temperature is reduced in AC_urban_1. ACM2_urban_1 thus predicts a higher temperature than ACM2_0.01 near the surface. Therefore, we can conclude that the difference in the near-surface temperature at the observation site at 08:00 LST between scenarios using different $K_{z\min}$ values can be attributed to the combined effect of the change in the local $K_{z\min}$ and the altering of $K_{z\min}$ in other areas through the advection process. This conclusion also holds for the simulated near-surface temperature at 15:00 LST shown in Fig. 7b.

Regarding TSK, in Fig. 6c and d we can see that the three features obtained in the analysis of T2 are also valid. The difference in TSK is larger in plain areas than in mountain areas, during the nighttime than during the daytime, and in urban areas than in areas with other land-use categories at night. But the difference in TSK is less than that of T2, indicating that the increase of $K_{z\min}$ exerts a less influence on TSK than on T2.

From Fig. 6e and f we can see that in most areas, when $K_{z\min}$ increases, HFX decreases during both the daytime and the nighttime, which represents that less heat is transferred from the surface to the atmosphere and that a larger amount of heat is transported from the atmosphere to the surface, respectively. Moreover, it was shown that the difference in HFX is larger in plain areas than in mountain areas. In addition, by comparing Fig. 6e and f, we found the boundary of the urban areas clearly discernible during the nighttime but unclear during the daytime. This shows that at nighttime the effects of changing $K_{z\min}$ on HFX in urban and non-urban areas are substantially different, while in the daytime the effects are similar.

3.4 Performance of ACM2_CMAQ and ACM2_0.01

We then adopted a function described in Eqs. (3)–(7) to calculate $K_{z\min}$ and compared the performance of the model (i.e., ACM2_CMAQ) with that using a constant $K_{z\min}$

Table 4. Statistical performances of ACM2_0.01 and ACM2_CMAQ in simulating T2.

Scenarios	RMSE	IOA	R	MB
ACM2_0.01	2.79	0.84	0.94	−2.49
ACM2_CMAQ	1.95	0.90	0.91	−1.44

(ACM2_0.01). The diurnal mean time series of T2, TSK, and HFX predicted by ACM2_CMAQ and ACM2_0.01 are shown in Fig. 8. From Fig. 8a, we can see that T2 predicted by ACM2_CMAQ is consistently higher than that predicted by ACM2_0.01, although it still underestimates the observations. It is also shown that the difference in T2 between ACM2_CMAQ and ACM2_0.01 increases at a lower T2, and the difference attains the greatest level when T2 reaches the lowest value in the morning. The difference in the minimum T2 between ACM2_CMAQ and ACM2_0.01 is 2.01 °C, while the deviation in the maximum T2 between these two scenarios is only 0.17 °C. As a result, the diurnal change of T2 using ACM2_CMAQ is smaller than that using ACM2_0.01. From Fig. 8b, it is shown that the behavior of the predicted TSK belonging to these two scenarios is similar to that of T2. ACM2_CMAQ predicts a higher TSK than ACM2_0.01, especially at night, and thus a smaller diurnal change of TSK. From Fig. 8c, we found that the difference in HFX between ACM2_CMAQ and ACM2_0.01 is larger at a negative HFX, while the difference is negligible at a positive HFX. When HFX is negative, the value of HFX predicted by ACM2_CMAQ is lower than that predicted by ACM2_0.01. This means that in the night simulations using ACM2_CMAQ, more heat is transferred from the atmosphere to the ground relative to the ACM2_0.01 scenario. This is caused by the enhanced vertical mixing within the boundary layer during the nighttime in the ACM2_CMAQ scenario, as the $K_{z\mathrm{min}}$ value given in ACM2_CMAQ is higher than that in ACM2_0.01. Table 4 summarizes the statistical performances of these two scenarios in simulating T2. It was found that the correlation coefficient (R) of ACM2_0.01 is higher than that of ACM2_CMAQ, which denotes that ACM2_0.01 predicts a better trend of the change in T2 than ACM2_CMAQ. However, the index of agreement (i.e., IOA) of ACM2_CMAQ is closer to 1.0 than that of ACM2_0.01, and the RMSE of ACM2_CMAQ is smaller than that of ACM2_0.01, denoting that the magnitude of T2 simulated by ACM2_CMAQ deviates less from the observation than that by ACM2_0.01.

Figure 9 shows the averaged vertical profiles of the potential temperature at 08:00 and 15:00 LST predicted by ACM2_0.01 and ACM2_CMAQ as well as the observations. It can be seen that at 08:00 LST, the difference in the potential temperature between these two simulation scenarios is remarkable near the ground. Below the height of 100 m, the potential temperature estimated by ACM2_CMAQ is higher

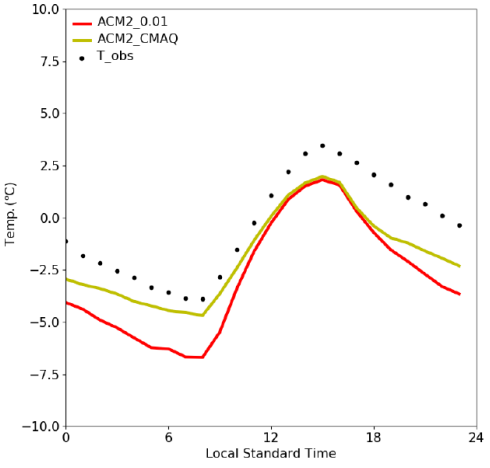

(a) temperature at 2 m (T2)

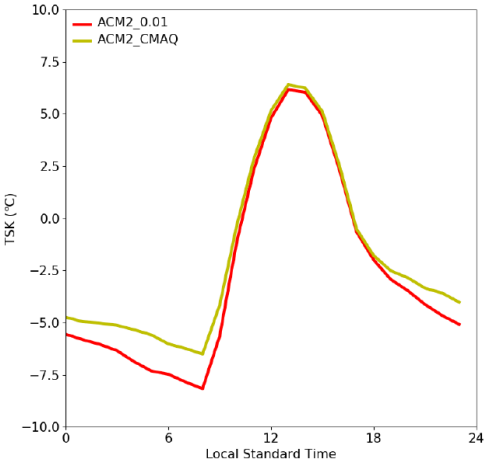

(b) surface skin temperature (TSK)

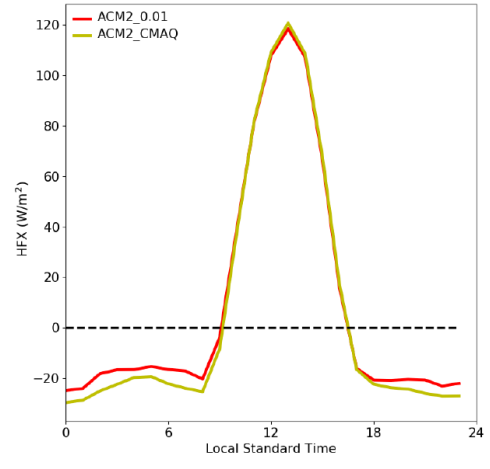

(c) sensible heat flux at the ground (HFX)

Figure 8. Diurnal mean time series of **(a)** T2, **(b)** TSK, and **(c)** HFX predicted by ACM2_CMAQ and ACM2_0.01.

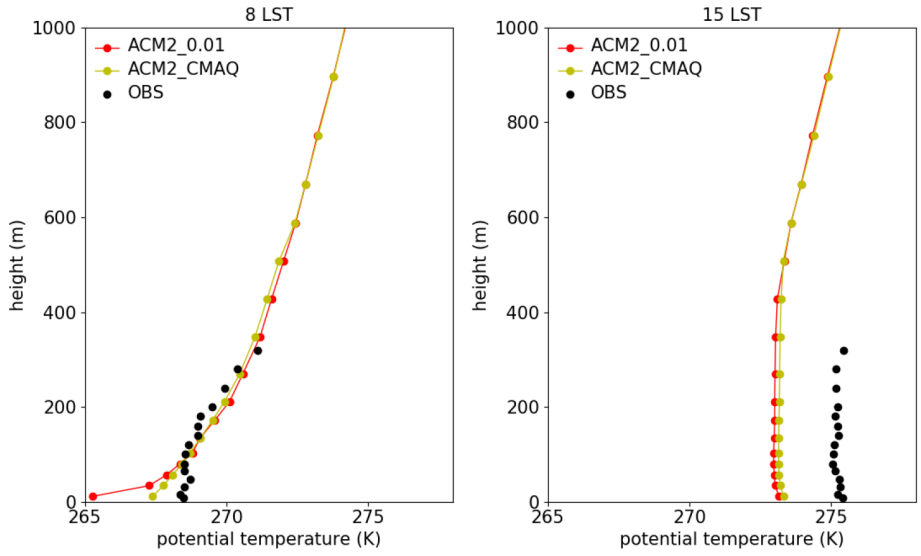

Figure 9. The vertical profiles of the potential temperature predicted by ACM2_0.01, and ACM2_CMAQ, and the observations at **(a)** 08:00 LST and **(b)** 15:00 LST averaged over the simulated days.

than that estimated by ACM2_0.01, and the largest difference (more than 2 K) occurs in the lowest layer of the model. In contrast, between the heights of 100 m and 500 m, the potential temperature predicted by ACM2_CMAQ is slightly lower than ACM2_0.01. The potential temperature gradient estimated by ACM2_CMAQ is thus smaller than that estimated by ACM2_0.01 below the height of 500 m. This different prediction of the vertical gradient of the potential temperature is because the turbulent mixing is very weak and $K_{z\min}$ dominates K_z at 08:00 LST. Moreover, the value of $K_{z\min}$ calculated by the function in ACM2_CMAQ is larger than that of ACM2_0.01 below the height of 500 m. Therefore, ACM2_CMAQ estimates a stronger vertical mixing, thus reducing the potential temperature gradient below the height of 500 m. In contrast, the profiles of the potential temperature predicted by these two scenarios are similar above the height of 500 m because of the equal $K_{z\min}$ values above 500 m in these two scenarios. By comparing the simulation results with the observations (see Fig. 9a), we found that ACM2_CMAQ estimates a closer potential temperature profile to the observations compared with ACM2_0.01, but it still overestimates the temperature gradient in the boundary layer at this time.

At 15:00 LST (see Fig. 9b) both the potential temperatures predicted by these two scenarios are about 2 K lower than the observations. The potential temperature predicted by ACM2_CMAQ is slightly higher than that predicted by ACM2_0.01 below the height of 500 m. Above 500 m, there is only a minor difference between ACM2_0.01 and ACM2_CMAQ. The reason is the same to that in the 08:00 LST simulation that above 500 m, the values of $K_{z\min}$ given in ACM2_0.01 and ACM2_CMAQ are equal.

The spatial distribution of the time-averaged differences of T2, TSK, and HFX between ACM2_CMAQ and ACM2_0.01 is shown in Fig. 10. From Fig. 10a–d, we can see that in urban areas, the difference in T2 and TSK between these two scenarios is mostly positive during both the daytime and the nighttime, which denotes that T2 and TSK predicted by ACM2_CMAQ are consistently higher than those predicted by ACM2_0.01 in urban areas. However, in non-urban areas the difference is minor. This is because compared with ACM2_0.01, ACM2_CMAQ uses a larger $K_{z\min}$ in urban and built-up areas below the height of 500 m. As a result, ACM2_CMAQ estimates a stronger vertical mixing in the PBL of urban areas than ACM2_0.01, thus resulting in an elevation of T2 and TSK. In contrast, in non-urban areas the $K_{z\min}$ values given in these two scenarios are identical (i.e., 0.01); the simulation results are thus similar. By comparing Fig. 10a and b, it can also be found that in urban areas the difference in T2 between ACM2_0.01 and ACM2_CMAQ during the nighttime is larger than that during the daytime, and this feature is also valid for the TSK deviation according to Fig. 10c and d. These results are consistent with the conclusions achieved above, stating that the change in $K_{z\min}$ has the largest impact on the variation of T2 and TSK in the nighttime of the urban areas. With respect to HFX, it was found in Fig. 10e that during the daytime the difference in HFX between ACM2_CMAQ and ACM2_0.01 is indiscernible. However, at nighttime (see Fig. 10f) the shapes of the urban areas are clearly indicated in the spatial distribution of the HFX deviation. This means that the HFX difference in

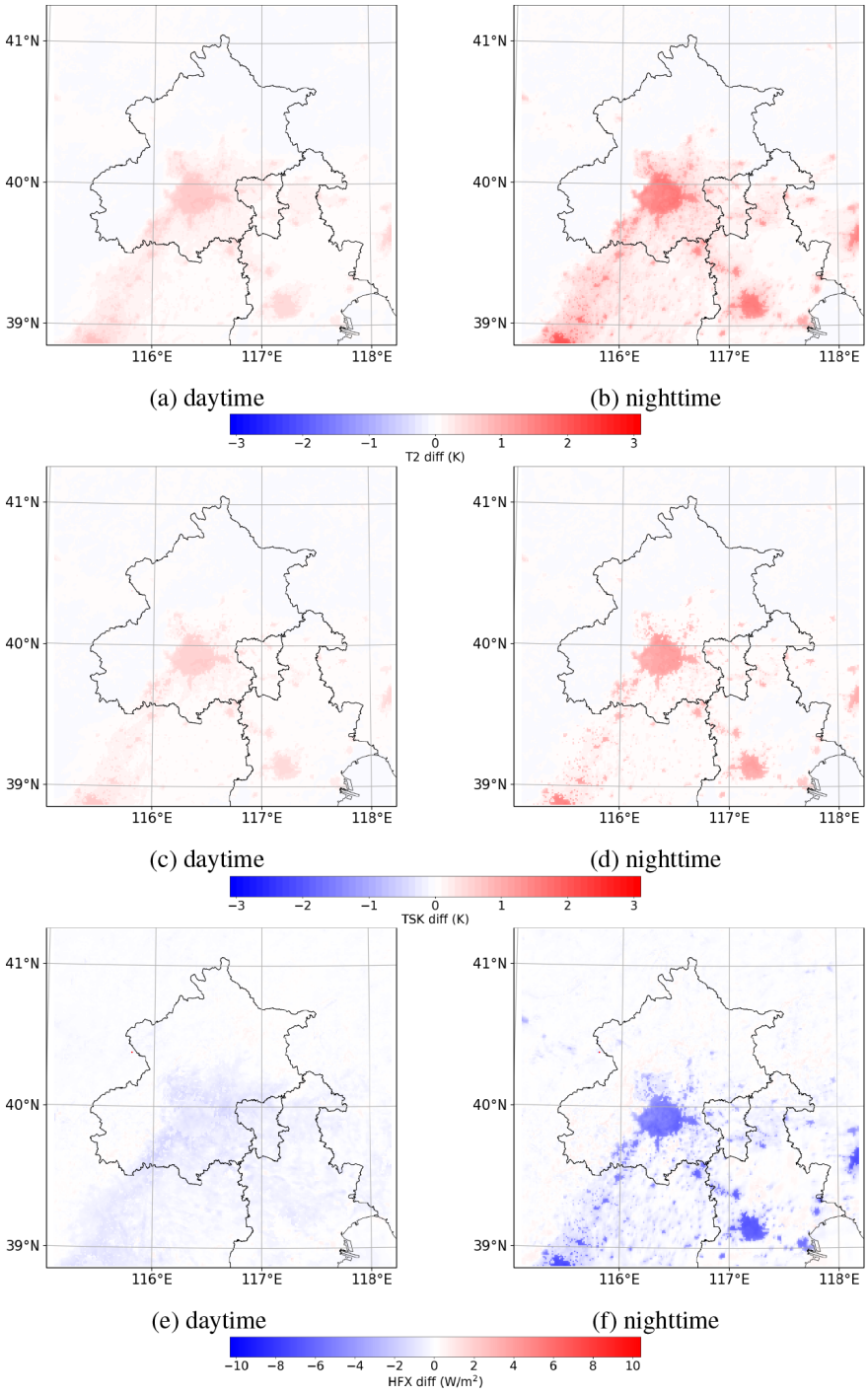

Figure 10. Spatial distribution of the mean differences (ACM2_CMAQ minus ACM2_0.01) in **(a, b)** T2, **(c, d)** TSK, and **(e, f)** HFX over daytime **(a, c, e)** and nighttime **(b, d, f)**.

urban areas between ACM2_0.01 and ACM2_CMAQ mostly exists during the nighttime. In addition, Fig. 10f also shows that during the nighttime the negative value of HFX in urban areas predicted by ACM2_CMAQ is lower than that provided by ACM2_0.01, which means that larger amount of heat is transferred from the atmosphere to the ground during the nighttime in the ACM2_CMAQ simulation.

4 Conclusions and future developments

In this study, we evaluated the performance of the ACM2 scheme with different $K_{z\min}$ settings in the estimation of the 2 m temperature (T2), surface skin temperature (TSK), and near-surface air temperature (T_level1) in the area of Beijing, China. We found that the change in $K_{z\min}$ in the ACM2 scheme can significantly influence the model performance in simulating these temperatures. Increasing $K_{z\min}$ leads to a remarkable elevation of T2 at night and a weakening of the diurnal change of T2. From the energy balance equation, we figured out that the mechanism for the elevation of T2 at night is because larger $K_{z\min}$ causes a significant enhancement of the turbulent mixing within the stable boundary layer at night. Thus, the enhanced mixing in the nighttime reduces the vertical gradient of the potential temperature within the boundary layer, and thus elevates the air temperature near the ground surface (i.e., T_level1). The elevation of the near-surface air temperature then decreases the nighttime sensible heat flux at the ground (i.e., HFX in the model), representing the fact that more heat is transferred from the atmosphere to the ground. As a result, the surface temperature (i.e., TSK) becomes higher. The elevations of TSK and T_level1 in the model consequently lead to the increase of the 2 m temperature (T2).

We also figured out the features of the influence of changing $K_{z\min}$ on the temperature prediction under different underlying surface categories. It was found that the impact on the 2 m temperature and the surface temperature brought by the change in $K_{z\min}$ is stronger during the nighttime than during the daytime, in plain areas than in mountain areas, and in urban areas than in non-urban areas at night.

When using a function calculating $K_{z\min}$ in the ACM2 scheme (i.e., the ACM2_CMAQ scenario), we found that the simulated 2 m temperature elevates in urban areas, compared with that using a constant $K_{z\min}$ (i.e., ACM2_0.01). The reason is the same as that in the nighttime simulation, larger $K_{z\min}$ in ACM2_CMAQ leads to a transport of more sensible heat from the atmosphere to the surface, resulting in a higher prediction of the 2 m temperature. In addition, the simulated vertical profiles of the potential temperature show that ACM2_CMAQ estimates a smaller potential temperature gradient than ACM2_0.01 within the boundary layer, especially at night, and the profile of the potential temperature given by ACM2_CMAQ is closer to the observation than that provided by ACM2_0.01. Moreover, the spatial distribution of the temperature deviation between these two scenarios shows that in the daytime the temperature simulated by ACM2_CMAQ is only slightly higher than ACM2_0.01 in both urban and non-urban areas. However, the difference becomes remarkable at nighttime in the urban areas.

The present study has some limitations. For instance, currently we lack observational data representing the surface energy balance and surface exchange fluxes, and these data may help to better evaluate the model performance. Moreover, in the present study, the influence of changing $K_{z\min}$ on the temperature prediction was investigated based on the ACM2 scheme. The role of $K_{z\min}$ in other PBL schemes such as YSU (Hong et al., 2006) and QNSE (Sukoriansky and Galperin, 2008; Sukoriansky et al., 2006) should also be studied in the future. In addition, the conclusions achieved in the present study are primarily valid for the area of Beijing, China. Thus, whether these conclusions are still valid in other areas, especially those with different categories of the underlying surface (i.e., sea, desert), also needs to be clarified.

In the future, more extended time periods are to be simulated so that the conclusions achieved in the present study can be verified more thoroughly. Moreover, the impacts of changing $K_{z\min}$ on the spatiotemporal distribution of other meteorological parameters such the wind and moisture will also be evaluated more thoroughly. In addition, we plan to assess the effects of changing $K_{z\min}$ on simulations of air pollution under different weather conditions, due to the strong connection between the diffusion of pollutants and the vertical turbulent mixing.

Code and data availability. The source code of WRF version 3.9.1.1 can be found on the following website: http://www2.mmm.ucar.edu/wrf/users/download/ (Skamarock et al., 2008). The code described by Eqs. (3)–(7), defining a functional-type $K_{z\min}$ in the ACM2 scheme of WRF, can be found in the directory named "Modified_WRF_Code" in the Supplement. The WRF model input namelist file and the post-processing python scripts are also available in the Supplement, named "WRF_namelist" and "post-processing-scripts", respectively. In addition, the observational data obtained from the meteorological observation tower and the observational system provided by the Institute of Atmospheric Physics, Chinese Academy of Sciences (IAP, CAS), are included in the directory "obs_data" of the Supplement.

Supplement. The supplement related to this article is available online at: https://doi.org/10.5194/gmd-14-6135-2021-supplement.

Author contributions. HD and LC conceived the idea of the article and ran the model. HD also wrote the python script for the data processing. LC and HD wrote the paper together. HJ and WJ revised the paper and gave valuable suggestions. YC and JA from IAP, CAS, provided the observational data and gave useful advice about the comparison of the model results with the observations. All the authors listed read and approved the final manuscript.

Competing interests. The contact author has declared that neither they nor their co-authors have any competing interests.

Acknowledgements. The authors would like to thank Holger Grosshans from Physikalisch-Technische Bundesanstalt (PTB) for revising this paper. The numerical calculations in this paper have been done on the high-performance computing system in the High-Performance Computing Center at the Nanjing University of Information Science and Technology.

Financial support. This research has been supported by the National Key R&D Program of China (grant no. 2017YFC0209801) and the National Natural Science Foundation of China (grant no. 41705103).

Review statement. This paper was edited by Leena Järvi and reviewed by two anonymous referees.

References

Angevine, W. M.: An Integrated Turbulence Scheme for Boundary Layers with Shallow Cumulus Applied to Pollutant Transport, J. Appl. Meteorol., 44, 1436–1452, 2005.

Angevine, W. M., Jiang, H., and Mauritsen, T.: Performance of an Eddy Diffusivity–Mass Flux Scheme for Shallow Cumulus Boundary Layers, Mon. Weather Rev., 138, 2895–2912, 2010.

Banks, R. F., Tiana-Alsina, J., Baldasano, J. M., Rocadenbosch, F., Papayannis, A., Solomos, S., and Tzanis, C. G.: Sensitivity of boundary-layer variables to PBL schemes in the WRF model based on surface meteorological observations, lidar, and radiosondes during the HygrA-CD campaign, Atmos. Res., 176, 185–201, 2016.

Bougeault, P. and Lacarrere, P.: Parameterization of orography-induced turbulence in a mesobeta–scale model, Mon. Weather Rev., 117, 1872–1890, 1989.

Broxton, P. D., Zeng, X., Sulla-Menashe, D., and Troch, P. A.: A global land cover climatology using MODIS data, J. Appl. Meteorol. Clim., 53, 1593–1605, https://doi.org/10.1175/JAMC-D-13-0270.1, 2014.

Byun, D. and Schere, K. L.: Review of the Governing Equations, Computational Algorithms, and Other Components of the Models-3 Community Multiscale Air Quality (CMAQ) Modeling System, Appl. Mech. Rev., 59, 51–77, https://doi.org/10.1115/1.2128636, 2006.

Chaouch, N., Temimi, M., Weston, M., and Ghedira, H.: Sensitivity of the meteorological model WRF-ARW to planetary boundary layer schemes during fog conditions in a coastal arid region, Atmos. Res., 187, 106–127, 2017.

Chen, F. and Dudhia, J.: Coupling an advanced land surface–hydrology model with the Penn State–NCAR MM5 modeling system. Part I: Model implementation and sensitivity, Mon. Weather Rev., 129, 569–585, 2001.

Chen, S.-H. and Sun, W.-Y.: A one-dimensional time dependent cloud model, J. Meteorol. Soc. Jpn., 80, 99–118, 2002.

Cuchiara, G. C., Li, X., Carvalho, J., and Rappenglück, B.: Intercomparison of planetary boundary layer parameterization and its impacts on surface ozone concentration in the WRF/Chem model for a case study in Houston/Texas, Atmos. Environ., 96, 175–185, 2014.

Du, Q., Zhao, C., Zhang, M., Dong, X., Chen, Y., Liu, Z., Hu, Z., Zhang, Q., Li, Y., Yuan, R., and Miao, S.: Modeling diurnal variation of surface PM2.5 concentrations over East China with WRF-Chem: impacts from boundary-layer mixing and anthropogenic emission, Atmos. Chem. Phys., 20, 2839–2863, https://doi.org/10.5194/acp-20-2839-2020, 2020.

Dudhia, J.: Numerical study of convection observed during the winter monsoon experiment using a mesoscale two-dimensional model, Journal of the Atmospheric Sciences, 46, 3077–3107, 1989.

Grell, G. A. and Dévényi, D.: A generalized approach to parameterizing convection combining ensemble and data assimilation techniques, Geophys. Res. Lett., 29, 38-1–38-4, 2002.

Grell, G. A., Peckham, S. E., Schmitz, R., McKeen, S. A., Frost, G., Skamarock, W. C., and Eder, B.: Fully coupled "online" chemistry within the WRF model, Atmos. Environ., 39, 6957 – 6975, https://doi.org/10.1016/j.atmosenv.2005.04.027, 2005.

Gunwani, P. and Mohan, M.: Sensitivity of WRF model estimates to various PBL parameterizations in different climatic zones over India, Atmos. Res., 194, 43–65, 2017.

Hong, S.-Y. and Pan, H.-L.: Nonlocal boundary layer vertical diffusion in a medium-range forecast model, Mon. Weather Rev., 124, 2322–2339, 1996.

Hong, S.-Y., Noh, Y., and Dudhia, J.: A new vertical diffusion package with an explicit treatment of entrainment processes, Mon. Weather Rev., 134, 2318–2341, 2006.

Hu, X.-M., Nielsen-Gammon, J. W., and Zhang, F.: Evaluation of three planetary boundary layer schemes in the WRF model, J. Appl. Meteorol. Clim., 49, 1831–1844, 2010.

Janjić, Z. I.: The step-mountain eta coordinate model: Further developments of the convection, viscous sublayer, and turbulence closure schemes, Mon. Weather Rev., 122, 927–945, 1994.

Kusaka, H., Kondo, H., Kikegawa, Y., and Kimura, F.: A Simple Single-Layer Urban Canopy Model For Atmospheric Models: Comparison With Multi-Layer And Slab Models, Bound.-Lay. Meteorol., 101, 329–358, 2001.

Li, D. and Bou-Zeid, E.: Quality and sensitivity of high-resolution numerical simulation of urban heat islands, Environ. Res. Lett., 9, 055001, https://doi.org/10.1088/1748-9326/9/5/055001, 2014.

Li, X. and Rappenglueck, B.: A study of model nighttime ozone bias in air quality modeling, Atmos. Environ., 195, 210–228, 2018.

Madala, S., Satyanarayana, A., and Rao, T. N.: Performance evaluation of PBL and cumulus parameterization schemes of WRF ARW model in simulating severe thunderstorm events over Gadanki MST radar facility – case study, Atmos. Res., 139, 1–17, 2014.

Mlawer, E. J., Taubman, S. J., Brown, P. D., Iacono, M. J., and Clough, S. A.: Radiative transfer for inhomogeneous atmospheres: RRTM, a validated correlated-k model for the longwave, J. Geophys. Res.-Atmos., 102, 16663–16682, 1997.

Moeng, C.-H., Dudhia, J., Klemp, J., and Sullivan, P.: Examining Two-Way Grid Nesting for Large Eddy Simulation of the PBL Using the WRF Model, Mon. Weather Rev., 135, 2295–2311, https://doi.org/10.1175/MWR3406.1, 2007.

Nakanishi, M. and Niino, H.: Development of an improved turbulence closure model for the atmospheric boundary layer, J. Meteorol. Soc. Jpn., 87, 895–912, 2009.

National Centers for Environmental Prediction, National Weather Service, NOAA, U.S. Department of Commerce: NCEP FNL Operational Model Global Tropospheric Analyses, continuing from July 1999, Research Data Archive at the National Center for Atmospheric Research, Computational and Information Systems Laboratory, Boulder, CO, USA, https://doi.org/10.5065/D6M043C6, 2000.

Nielsen-Gammon, J. W., Hu, X.-M., Zhang, F., and Pleim, J. E.: Evaluation of planetary boundary layer scheme sensitivities for the purpose of parameter estimation, Mon. Weather Rev., 138, 3400–3417, 2010.

Olson, J. B., Kenyon, J. S., Angevine, W., Brown, J. M., Pagowski, M., and Sušelj, K.: A description of the MYNN-EDMF scheme and the coupling to other components in WRF–ARW, Tech. rep., NOAA Technical Memorandum OAR GSD-61, 2019.

Pleim, J. E.: A combined local and nonlocal closure model for the atmospheric boundary layer. Part I: Model description and testing, J. Appl. Meteorol. Clim., 46, 1383–1395, 2007a.

Pleim, J. E.: A combined local and nonlocal closure model for the atmospheric boundary layer. Part II: Application and evaluation in a mesoscale meteorological model, J. Appl. Meteorol. Clim., 46, 1396–1409, 2007b.

Pleim, J. E. and Chang, J. S.: A non-local closure model for vertical mixing in the convective boundary layer, Atmos. Environ., 26, 965–981, 1992.

Poulos, G., Blumen, W., Fritts, D., Lundquist, J., Sun, J., Burns, S., Nappo, C., Banta, R., Newsom, R., Cuxart, J., Terradellas, E., and Balsley, B.: CASES99: A Comprehensive Investigation of the Stable Nocturnal Boundary Layer, Bulletin of The American Meteorological Society, B. Am. Meteorol. Soc., 83, 555–582, https://doi.org/10.1175/1520-0477(2002)083<0555:CACIOT>2.3.CO;2, 2002.

Shin, H. H. and Hong, S.-Y.: Intercomparison of planetary boundary-layer parametrizations in the WRF model for a single day from CASES-99, Boundary-Layer Meteorology, 139, 261–281, 2011.

Shin, H. H. and Hong, S. Y.: Representation of the Subgrid-Scale Turbulent Transport in Convective Boundary Layers at Gray-Zone Resolutions, Mon. Weather Rev., 143, 250–271, 2015.

Skamarock, W., Klemp, J., Dudhia, J., Gill, D., Barker, D., Wang, W., and Powers, J.: A Description of the Advanced Research WRF Version 3, NCAR Technical Note, Tech. Rep. NCAR/TN–475+STR, National Center for Atmospheric Research, Boulder, CO, available at: http://www2.mmm.ucar.edu/wrf/users/download/ (last access: 2 November 2019), 2008.

Steeneveld, G., Van de Wiel, B., and Holtslag, A.: Modelling the Arctic stable boundary layer and its coupling to the surface, Bound.-Lay. Meteorol., 118, 357–378, https://doi.org/10.1007/s10546-005-7771-z, 2006.

Stull, R. B.: An Introduction to Boundary Layer Meteorology, vol. 13, Springer Science & Business Media, 1988.

Sukoriansky, S. and Galperin, B.: A Quasi-Normal Scale Elimination Theory of Turbulent Flows With Stable Stratification, in: Volume 4: Fatigue and Fracture; Fluids Engineering; Heat Transfer; Mechatronics; Micro and Nano Technology; Optical Engineering; Robotics; Systems Engineering; Industrial Applications, Engineering Systems Design and Analysis, 179–183, https://doi.org/10.1115/ESDA2008-59149, 2008.

Sukoriansky, S., Galperin, B., and Perov, V.: A quasi-normal scale elimination model of turbulence and its application to stably stratified flows, Nonlin. Processes Geophys., 13, 9–22, https://doi.org/10.5194/npg-13-9-2006, 2006.

Udina, M., Sun, J., Kosović, B., and Soler, M. R.: Exploring vertical turbulence structure in neutrally and stably stratified flows using the weather research and forecasting–large-eddy simulation (WRF–LES) model, Bound.-Lay. Meteorol., 161, 355–374, 2016.

Willmott, C. J.: Some comments on the evaluation of model performance, B. Am. Meteorol. Soc., 63, 1309–1313, 1982.

Xie, B., Fung, J. C., Chan, A., and Lau, A.: Evaluation of nonlocal and local planetary boundary layer schemes in the WRF model, J. Geophys. Res.-Atmos., 117, D12103, https://doi.org/10.1029/2011JD017080, 2012.

Zhang, D. and Anthes, R. A.: A high-resolution model of the planetary boundary layer – Sensitivity tests and comparisons with SESAME-79 data, J. Appl. Meteorol., 21, 1594–1609, 1982.